15TH IEA HEAT PUMP CONFERENCE
MAY 26–29, 2026 | HOFBURG
VIENNA 2026
DECARBONISATION THROUGH INNOVATION

Geometric Tweaks, Big Gains: Unlocking Heat Pump Efficiency Through Integrated Evaporator Design

Moritz Beckschulte *[a], Jonas Klingebiel [a], Stephan Göbel [a], Christian Vering [a], Dirk Müller [a]

[a]Institute for Energy Efficient Buildings and Indoor Climate, RWTH Aachen University, Mathieustraße 10, 52064 Aachen, Germany

Abstract

Frost formation on air-source heat pump evaporators yields efficiency losses during their operation under certain temperature and humidity conditions. Today, frosting phenomena are often neglected during the evaporator design process, resulting in additional efficiency losses during operation. In the literature, integrating the (de)frosting process into the evaporator design enhances efficiency during operation.

This paper investigates the influence of evaporator design on the operational performance of heat pumps, concerning frosting behavior in dynamic simulation studies. The underlying simulation model captures interactions between evaporator design (fin spacing, refrigerant-carrying tubes, and required installation space) and frosting behavior (influence on heat transfer and air-side pressure loss). Using a sensitivity analysis with respect to fin spacing, the model computes the energy efficiency in three different case studies (high humidity, average, and low humidity).

The results demonstrate a potential for improvement of the cycle efficiency of up to 10 %, depending on operating conditions. In all, the findings highlight the importance of integrated design approaches considering geometric parameters in evaporator design and refrigerant cycle control to mitigate frosting and enhance energy efficiency. Therefore, considering the effects of frost formation in the design process contributes to increasing the efficiency of air-source heat pumps in the field.

Keywords: Frost; Defrosting; Optimization; Fin and Tube; Heat Exchange, Mass Transfer; Modelling; Air-Source

1. Introduction

Air-source heat pumps (ASHPs) have become the dominant segment of the European heat pump market, accounting for 80 % of installations in 2024, primarily because of their comparatively low investment costs relative to alternative heat sources [1]. Their widespread adoption, however, brings focus to a well-known limitation: in cold and humid conditions, evaporator frost formation degrades the heat pump performance, constraining both heating capacity and efficiency at high heating demands. As a result, practical operation of ASHPs in such climates necessarily involves periodic defrosting to reset heat transfer capability and, thus, thermal capacity.

Frost formation is a transient effect of coupled heat and mass transfer at the air-coil interface, dependent on the refrigerant cycle conditions and its control [2]. Improved heat transfer on the evaporator side raises the evaporating temperature, which in turn reduces frost formation. Conversely, large temperature differences between the coil surface and the ambient air enhance frost growth.

Specific cycle configurations, such as the inclusion of an internal heat exchanger, can achieve increases in evaporating temperature for a given load [3]. Similarly, control strategies that minimize superheat can reach higher evaporating temperatures [4], thereby reducing frosting tendencies under otherwise identical ambient conditions. When frosting is unavoidable, reverse-cycle defrosting yields the highest cycle-averaged efficiency relative to hot-gas, electric-resistance, or warm-brine defrosting alternatives [5].

A range of countermeasures exists to mitigate frosting. These include geometric optimization of the evaporator, surface coatings, improved control decisions, and modifications to the refrigerant cycle configuration [2], [6], [7]. However, current practice often proceeds sequential design processes: an evaporator design is selected first based on thermal demands, and control is subsequently tuned for that specific design.

Several commercial calculation environments provide analysis of refrigerant cycles and heat exchangers, but do not natively model frosting and the implications on the refrigerant cycle. For example, Coil Designer coupled with the VapCyc library enables detailed heat exchanger geometries linked to cycle analysis [8]; EVAP-COND offers finned-tube evaporator modeling with capabilities for refrigerant circuitry optimization [9]; and IMST-ART supports cycle analysis and heat exchanger design studies [10]. These tools facilitate geometry-cycle co-analysis under dry-coil conditions, yet they do not capture frost growth and defrost.

The literature focuses on optimization in the absence of frosting. Circuitry optimization has been surveyed comprehensively (see Hu et al. [11]). Hou et al. presented a multi-objective optimization of a fin-and-tube heat exchanger, including structural parameters (e.g., tube count and spacing), circuitry, and volumetric air-flow parameters (fan speed); fin pitch and fin geometries were not included in that study. Reported efficiency improvements were as high as 30 % relative to the baseline [12]. Jing et al. combined circuitry and fin pitch optimization for an air conditioner using EVAP-COND, achieving reductions in friction factor and increases in the Colburn factor relative to the reference design [13]. These contributions demonstrate the leverage available from geometry and circuitry, but they exclude frosting, and thus, do not resolve the design trade-offs that emerge under cold, humid operation. These decoupled workflows contradict the strong interactions among geometry, cycle operation, and control logic that govern coil surface temperatures, air-side conditions, and, thus, frost formation. Accordingly, design, frosting, and control should be developed together, in an integrated manner, to fully realize system-level efficiency gains. Vering et al. showed integrated design approaches can be used to optimize system design and operation of heat pumps simultaneously to reduce operation costs of up to 36 % [14].

Studies that incorporate frosting reveal shifts in optimal designs once cycle-frost coupling is considered. Ribeiro et al. optimized the number of fins at a single operating point using quasi-steady-state simulations of an evaporator under frosting, coupled to a refrigerant cycle model, with total energy consumption as the objective. Notably, the system-level coupling shifted the optimal solution relative to evaporator-only analysis. However, experimental validation was limited to a single heat exchanger [15]. Yang et al. investigated fin spacing optimization for a refrigeration application across varied environmental conditions using two different optimization methods, reporting increases in average heat transfer rate of up to 13 % versus a reference model [16]. Taken together, these studies indicate that frosting-dependent optimization may alter design decisions. However, results from the literature are limited to specific geometries or discrete conditions.

While the literature provides several building blocks to focus on single effects (evaporator design, control, frosting), there is no integrated design approach simultaneously considering the three main effects: First, refrigerant-cycle models exist that explicitly represent interactions among the cycle, heat source and sink, and control decisions [17]. Second, a variety of frost growth models are available for different geometries and levels of detail. Third, dynamic studies of transient frosting have been conducted, though typically constrained to fixed geometries or single operating conditions [6], [18], [19], [20].

To evaluate the improvements in energy efficiency due to integrated design, there is no standardized method on EU level, yet. Recent testing conditions are defined that the native control algorithm is avoided, thus, yielding the suppression of frosting in energy label tests. Therefore, there is initiative to renew testing conditions that allow for interaction with the native heat pump controller [21].

The transient operation which is covered by a native heat pump controller in the field resulting from frost growth is not covered by standard test, yet [22]. Thus, heat pump control, frosting behavior, and the efficiency of defrost strategies have no impact on labelling procedure.

What remains insufficiently addressed are simulations that combine (i) time-varying boundary conditions, (ii) alternative evaporator geometries, and (iii) an explicit weighting of operating points reflecting their real-world frequency of occurrence. From a system-efficiency perspective, an optimal design must balance the trade-off between robustness under frosting conditions and high efficiency already during energy labeling.

1.1. Objectives and scope

This work addresses the above gaps by coupling dynamic system simulation with geometry variation and control under frosting:

- We develop a dynamic simulation model of a heat pump system, including a backup heater for capacity shortfall, coupled to a simplified building thermal model, with the aim of evaporator geometry optimization.
- We conduct sensitivity analysis of the evaporator geometry, focusing on fin pitch as the principal decision variable, and evaluate heating cycles across operating conditions from −10 °C to 12 °C and relative humidities from 59 to 97 %.
- We analyze the integrated design potential regarding control decisions, evaporator geometry, and building dynamics, with particular emphasis on fin pitch.

By explicitly modeling frosting and defrosting dynamics, control actions (e.g., superheat management and defrost initiation), and the building load, the study targets an integrated approach in which evaporator geometry and control are selected simultaneously. In doing so, we target the system-level optimum with integrated design approaches compared to sequential design procedures for air-source heat pumps.

2. Methods

To investigate the coupled effects of evaporator geometry and control on air-source heat pump performance under frosting conditions, a dynamic simulation-based approach was developed. The approach integrates a detailed heat pump system model with a simplified building thermal model, enabling the analysis of system behavior under realistic, time-varying loads. The entire heat pump system was modeled using the Modelica-based TIL-Suite library [17].

2.1. Heat Pump System Model

The core of this study is a model of an air-source heat pump, representing a standard vapor-compression cycle configuration as depicted in Figure 1. The model comprises the main refrigerant-side components, air-side components, water-site components and a frost growth model.

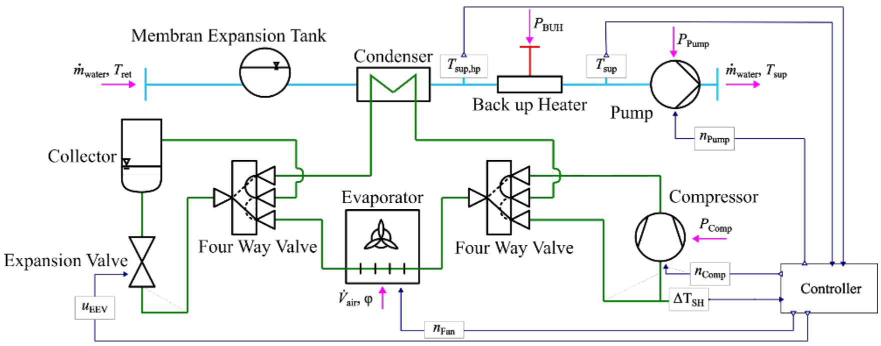

Figure 1. Schematic representation of the modelled heat pump system. The refrigerant and hydraulic (water) circuits are distinguished by green and light blue lines, respectively. Dark blue lines indicate the controller's input and output signals, while pink arrows denote the exchange of variables with the building model.

2.1.1. Refrigerant Cycle and Components

The refrigerant cycle consists of a compressor, a plate heat exchanger serving as the condenser, an isenthalpic expansion valve, and a collector. To specifically isolate the influence of the evaporator geometry, simplifying assumptions were made for key components. The compressor is modeled with constant isentropic, volumetric, and effective isentropic efficiencies, as specified in Table 1. Furthermore, the refrigerant-side pressure drop within the heat exchangers is neglected to enhance computational speed.

2.1.2. Evaporator and Frost Model

The evaporator is modeled as a fin-and-tube, cross-flow heat exchanger (HX) using the component models available in the TIL-Suite library. The air-side pressure drop is calculated using the correlation from Haaf [23], without the application of a correction factor. The geometric parameters of the baseline evaporator are detailed in Table 1.

A critical element of the simulation framework is the modeling of frost formation. A constant porosity frost model from the TIL-Suite [17] was employed. This model represents the accumulation on the fin surface as a composite of a liquid water layer and a solid frost layer, each with a fixed density. The total film density is dynamically computed based on a mass balance between the liquid and frost phases. The model accounts for the phase change energy associated with freezing and melting, as well as the corresponding changes in film volume, thermal conductivity, and the resulting increase in heat and mass transfer resistance on the air side. The actual air volume flow rate through the evaporator is determined dynamically at the intersection of the fan's characteristic curve (Table 2) and the calculated air-side pressure drop of the finned-tube heat exchanger. Therefore, any increase in pressure drop, either from geometry (smaller fin pitch) or frost accumulation, results in a reduced air volume flow rate.

Table 1. Refrigerant Cycle parameters.

Parameter	Value and unit
Compressor displacement	30 cm^3
Compressor Efficiency	0.7
Capacity BUH	6200 W
Finned Tube Length (HX width)	0.6 m
Number of Serial Tubes	3
Distance between serial tubes	22 mm
Number of parallel tubes	25.4 mm
Thickness of fins	0.2 mm
Distance between fins	5 mm

Table 2. Fan Characteristics.

Parameter	Value and unit
Nominal fan speed	13 Hz
Nominal pressure increase at nominal speed	10 Pa
Nominal Volume Flow Rate	0.639 m^3/s
Volume Flow Rate at nominal speed without pressure drop	0.7 m^3/s

2.1.3. Auxiliary Components

The system model includes an outdoor fan and a backup heater (BUH) to ensure the heating demand is met under all conditions. The fan is represented by a characteristic curve, with its nominal operating parameters provided in Table 2. The BUH is modeled as an ideal electrical resistance heater, providing an instantaneous thermal response to its control signal with a maximum capacity as listed in Table 1.

2.2. System Control Logic

A rule-based control strategy governs the heat pump's operation, switching between three distinct modes: normal heating, defrost, and cycling (off-mode). The transitions between these modes are triggered by predefined thresholds. To ensure a consistent basis for comparison across all geometric variations, the control logic and its parameters were held constant throughout all simulations.

- **Normal Heating Mode:** The compressor speed is modulated by a PI controller to maintain the desired supply water temperature. The expansion valve is also managed by a PI controller to regulate superheat to a constant value of 10 K.
- **Defrost Mode:** Defrost is initiated when the accumulated frost mass on the evaporator reaches a threshold of 1.5 kg. During this mode, the cycle is reversed. The compressor operates at a fixed speed, the expansion valve is fully opened, and the water pump speed is increased to facilitate rapid melting. Defrost is terminated once the evaporator fin surface temperature exceeds 20 °C.
- **Cycling Mode:** If the building heat demand falls below the minimum heating capacity of the unit, causing the supply temperature to exceed its upper threshold, the compressor is switched off and the system enters a low-power cycling state. The system resumes normal heating when the supply temperature drops below the lower threshold as indicated in Table 3.

The backup heater is controlled by a three-step PI controller and is disabled during defrost. It is permitted to activate only if the supply temperature remains below its setpoint for a duration of two minutes while the compressor is already operating at a high speed (above 95 Hz). A summary of the key control parameters for each operational mode is provided in Table 3.

2.3. Building Load Simulation

To represent the dynamic thermal load and create a realistic closed-loop interaction, the heat pump model was coupled with a simplified building model. A two-mass model (2MM, 2R-2C), as described in [21], was utilized. This model represents the building's thermal dynamics through two coupled thermal masses: a "fast" mass representing the indoor air and heat distribution system, and a "slow" mass representing the building envelope and furniture.

The heat pump model delivers thermal energy to the inner (fast) mass of the 2MM. The 2MM, in turn, calculates the evolution of the indoor and envelope temperatures based on energy balances, including heat transfer between the masses and to the ambient environment. Crucially, the model computes a dynamic water return temperature based on the state of the inner mass, which is then fed back to the heat pump model. This closed-loop coupling ensures that the heat pump's operation continuously adapts to the building's thermal response.

Table 3. Control parameters at different operational phases.

Parameter	Normal	Defrost	Cycling
Initiation	-	Frost mass above 1,5 kg	Supply temperature to high: ($T_{\mathrm{sup,set}} + 2{,}5$ K)
Termination	-	Fin temperature above 20 °C	Supply temperature to low ($T_{\mathrm{sup,set}} - 2{,}5$ K)
Compressor speed	PI controller (30 Hz to 100 Hz)	60 Hz	Off (2 Hz)
Fan Speed	10 Hz	1 Hz	1 Hz
Expansion Valve	PI controller	Fully opened	
Pump speed	0.2 kg/s	0.3 kg/s	0.1 kg/s
Back Up Heater	Three step PI controller	Off	Off

For the simulation, the Modelica-based heat pump model was exported as a Functional Mock-up Unit (FMU) and coupled with the 2MM, which was implemented in Python. The co-simulation was performed using the CVODE solver with a relative tolerance of 1e-4 and a communication step size of one second.

2.4. Simulation Procedure and Test Conditions

The investigation was structured as a parametric sweep to evaluate the influence of a key geometric variable on system performance across a range of representative operating conditions.

The evaporator fin pitch was varied from 1 mm to 7 mm in 1 mm increments while the outer dimensions of the heat exchanger were not changed. For each geometric configuration, the heat pump system was simulated at five distinct ambient test points, as defined in the standard EN 14511 and detailed in Table 4. These points span a temperature range from -10 °C to 12 °C, covering conditions prone to heavy frosting, moderate frosting, and no frosting.

To ensure that the analyzed data were free from initialization transients, each simulation was run for at least two full operational cycles, with data being recorded only from the second cycle onward. An "operational cycle" was defined based on the dominant system behavior at a given test point:

- At low ambient temperatures where frosting is significant, a cycle consists of one full frosting and subsequent defrost period.
- At milder ambient temperatures where the heat demand is below the minimum unit capacity, a cycle consists of one on/off period.
- At intermediate conditions where the heat pump operates continuously without frosting or cycling, a ten-hour period of steady operation is defined as a cycle.

At the end of section 3, a sensitivity analysis is performed to evaluate the influence of ambient humidity φ on the results. Since field measurements indicate that actual relative humidity often varies over a wider range and reaches higher levels than those prescribed in standard tests [24], simulations are repeated with humidity values 10 % higher and lower than the nominal values in Table 4. This analysis quantifies the robustness of the optimal fin pitch selection against variations in local climate conditions, which correspond to different installation sites.

Table 4. Ambient temperature, relative humidity, heating load and supply set temperature for the analyzed test points.

Test point	Ambient temperature	Relative Humidity	Heating load	Supply set temperature
E	−10 °C	69 %	6200 W	55 °C
A	−7 °C	75 %	5485 W	52 °C
B	2 °C	84 %	3339 W	42 °C
C	7 °C	87 %	2146 W	36 °C
D	12 °C	89 %	954 W	30 °C

2.5. Efficiency metrics and Diagnostic Variables

To quantify and compare the performance of different evaporator geometries, two primary metrics were used: the cycle-averaged Coefficient of Performance ($\overline{COP}_{\text{Cycle}}$) and the Seasonal Coefficient of Performance ($SCOP$). The $\overline{COP}_{\text{Cycle}}$ provides a fair basis for comparison at a single operating point by accounting for all energy consumption and heat delivery over a complete operational cycle. It is calculated as:

$$\overline{COP}_{\text{Cycle}} = \frac{Q_{\text{total}}}{W_{\text{total}}} = \frac{\int_{\text{Cycle}} \dot{Q}_{\text{Cond}} + P_{\text{BUH}}}{\int_{\text{Cycle}} P_{\text{Comp}} + P_{\text{BUH}} + P_{\text{Fan}} + P_{\text{Pump}}} \quad (1)$$

where $\dot{Q}_{\text{Cond}}$ is the condenser heating power, and P_{BUH}, P_{Comp}, P_{Fan}, and P_{Pump} are the electrical power consumption of the backup heater, compressor, fan, and water pump, respectively. The integration period, Cycle, corresponds to one full frost-defrost period, one on-off cycle, or a ten-hour steady-state period, as defined in Section 2.4.

The $SCOP$ serves as the key metric for overall system efficiency across an entire heating season. It was calculated according to the bin-hour method specified in EN 14511 [22] for the "average" climate zone. The $SCOP$ is defined as:

$$SCOP = \frac{\sum_{15\,°C}^{T=-10\,°C} h_{T_i} \cdot Q_{\text{total},T_i}}{\sum_{15\,°C}^{T=-10\,°C} h_{T_i} \cdot W_{\text{total},T_i}} \quad (2)$$

where h_{T_i} is the number of hours per year (bin hours) that the ambient temperature T_i occurs, and Q_{total,T_i} and W_{total,T_i} are the total heat delivered and total work consumed during a representative cycle at test point, as derived from Equation (1).

To analyze the physical mechanisms responsible for performance differences, several diagnostic variables were evaluated. These include the air volume flow rate through the evaporator $\dot{V}_{\text{air}}$, which indicates the aerodynamic penalty from geometry and frost blockage, and the overall heat transfer coefficient $k \cdot A$, which quantifies the evaporator's thermal performance, including the insulating effect of the frost layer. Additionally, system temperatures (supply, return, and heat pump outlet) were analyzed to illustrate the dynamic interactions between the heat pump, its controls, and the building load.

3. Results and Discussion

The simulation results provide insight into the system's behavior. The interaction between the evaporator geometry, control logic, and building load yields operational patterns, particularly at the extremes of the tested temperature range. The following sections describe the characteristic behavior observed during defrost-dominated operation and cycling operation.

We analyze the impact of changing the fin pitch under the test point conditions shown in Table 4. The volume flow rate of air through the evaporator and the overall heat transfer coefficient are used to describe the interactions of design decisions on transient operation that occur due to the integrated design approach.

Finally, the results of the sensitivity analysis of the relative humidity are presented.

3.1. Interaction of heat pump model with two mass model

Figure 2 illustrates the characteristic system dynamics during a complete frost-defrost cycle at the -7 °C test point (PLC-A), which is representative of operation at PLC-E and PLC-B as well. The cycle starts following the termination of the preceding defrost sequence, which occurs when the evaporator fin temperature reaches 20 °C, switching the four-way valve to heating mode.

Initially, the control system drives the heat pump to its maximum capacity to reach the supply temperature. Due to the high thermal demand at this low ambient temperature, the backup heater (BUH) is activated to meet the supply temperature setpoint. The heat pump's supply temperature $T_{\mathrm{sup,hp}}$ (orange curve) stabilizes after around 40 minutes due to constant (maximum) compressor speed. The BUH is switched on to increase the supply temperature T_{sup} (red curve) to the desired value and begins to cycle between its lowest capacity and off, resulting in oscillations in the supply temperature in the red curve of Figure 2. The control interaction is a response characteristic of the building's thermal masses: an initial rapid drop followed by a slower decline, reflecting the coupled thermal dynamics of the heat pump and the building model.

Over time, frost accumulates on the evaporator fins due to the ambient air conditions. This process progressively increases the thermal and aerodynamic resistance on the evaporator air side, leading to a gradual degradation of the system's heating capacity. This degradation results in a heat pump's supply temperature decrease (orange curve).

When the accumulated frost mass reaches the predefined 1.5 kg threshold, the defrost sequence is initiated. The refrigerant cycle is reversed, causing the supply temperature to drop sharply as the unit temporarily extracts heat from the building's hydraulic system, resulting in the return temperature exceeding the supply temperature. This extracted heat melts the frost, which then drains from the evaporator, resetting its heat transfer capability for the next heating cycle.

When no frost is formed (at low loads and air temperatures well above 0 °C) further system interaction can be observed. Operation at the 12 °C test point (PLC-D), shown in Figure 3, is characterized by cycling. The cycle begins with the compressor operating at its lowest permissible speed. Because the heating capacity at this speed exceeds the load, the supply temperature gradually increases.

Once the supply temperature reaches the upper control threshold at 32.5 °C (setpoint + 2.5 K hysteresis, at around 0.3 hours), the controller initiates the shutdown sequence. The compressor speed is ramped down to 2 Hz (a non-zero value maintained for the numerical stability of the model). A notable dynamic effect occurs at this transition: a peak in the supply temperature. This is caused by the circulation pump's mass flow rate decreasing more rapidly than the compressor ramps down its speed, a consequence of the implemented maximum gradient for compressor speed change. With the compressor effectively off, both the supply and return temperature steadily decrease as the building continues to exchange heat with the hydraulic loop and the ambient. When the supply temperature falls to the lower control threshold of 27.5 °C (setpoint – 2.5 K hysteresis), the compressor is switched back on, initiating the next heating phase.

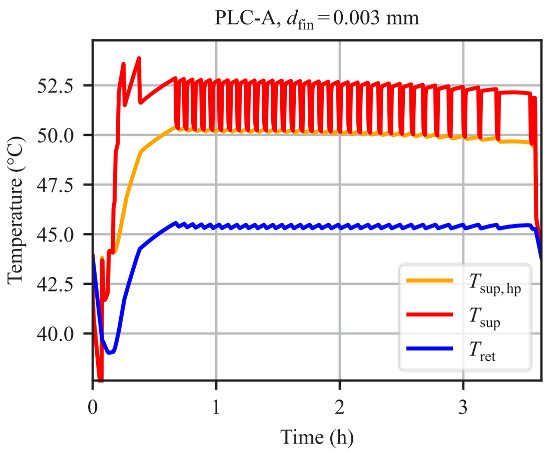

Figure 2. Temperatures for defrosting test point (PLC-A).

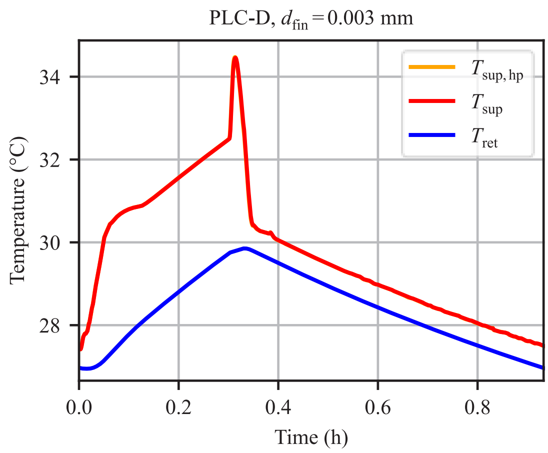

Figure 3. Temperatures for cycling test point (PLC-D).

It is noteworthy that the simulated dynamics, such as the necessity of the backup heater post-defrost and the system's cycling behavior at low loads, are consistent with empirical observations from laboratory tests of physical heat pumps.

3.2. Impact of fin pitch variation

Under non-frosting conditions (test point PLC-D), the choice of fin pitch involves a trade-off between two competing loss mechanisms, with air-side thermal resistance being the dominant factor. As illustrated in Figure 4, the violin plots show narrow data distributions, indicating stable performance, with outliers attributable to compressor speed adjustments.

The first loss mechanism is airflow restriction. Decreasing the fin pitch reduces the hydraulic area, which increases pressure drop. Since the fan operates at discrete speeds, this results in a lower air volume flow rate. To maintain the required evaporator capacity with less air, the temperature difference across the coil must increase, which forces the evaporation temperature down and lowers the $\overline{COP}_{\text{Cycle}}$.

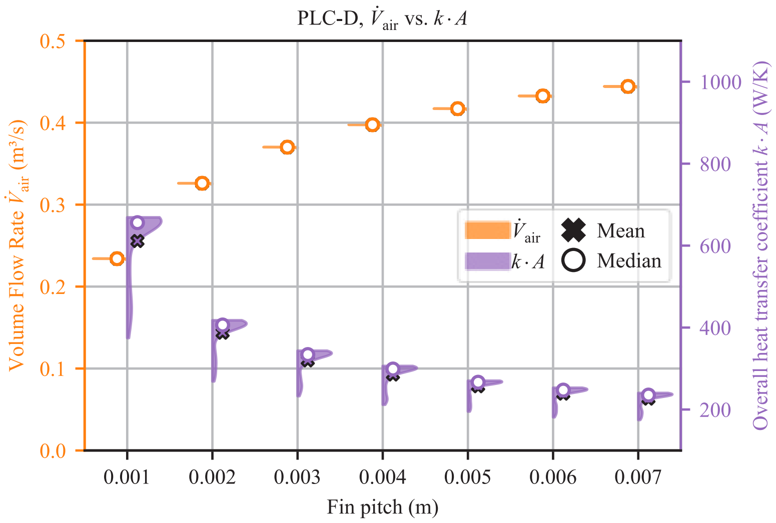

Figure 4. Volume Flow Rate $\dot{V}_{\text{air}}$ und overall heat transfer coefficient $k \cdot A$ for different fin pitches during the on phase of one cycle without frosting (PLC-D).

The second mechanism relates to heat transfer. The overall heat transfer coefficient is highly dependent on fin pitch. A small 1 mm pitch provides a large surface area, yielding an overall heat transfer coefficient of approximately 600 W/K. Conversely, a large 7 mm pitch has a much smaller area, resulting in a $k \cdot A$ of only 130 W/K. A low overall heat transfer coefficient requires a larger temperature difference between the refrigerant and the air to transfer the same amount of heat, which again lowers the evaporation temperature and, consequently, the $\overline{COP}_{\text{Cycle}}$.

When frost forms (test point PLC-A, Figure 5), it amplifies both loss mechanisms by simultaneously blocking airflow and adding a layer of thermal insulation. The loss mechanism that is already dominant for a specific fin pitch is the one that increases most significantly during frosting.

- **Airflow Blockage:** The absolute reduction in air volume flow rate is similar across all pitches (around 0.2 m³/s). However, the relative impact is far more severe at smaller pitches. At the point of defrost initiation, a 1 mm pitch results in a 70 % reduction in airflow, whereas a 7 mm pitch only results in a 50 % reduction. This drastic flow reduction lowers the evaporation temperature and system efficiency.
- **Thermal Insulation:** The insulating effect of frost is more pronounced at larger fin pitches. The wider spacing allows a thicker, less dense frost layer to accumulate, which causes a greater reduction in the overall heat transfer coefficient.

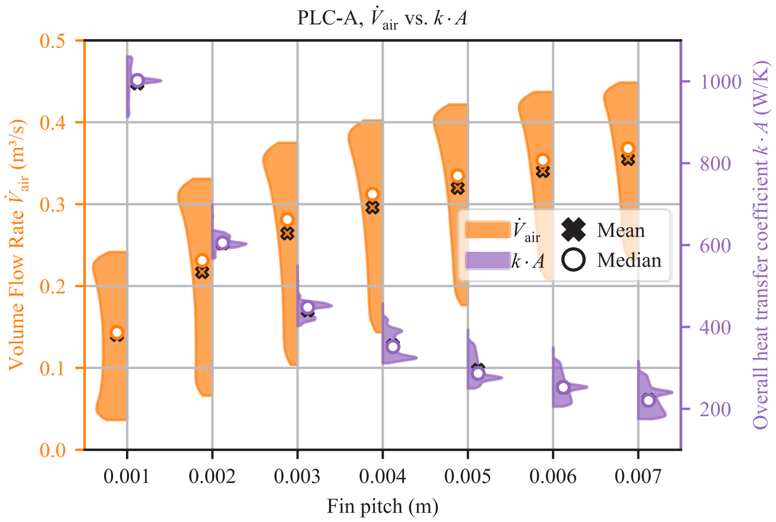

Figure 5. Volume Flow Rate $\dot{V}_{air}$ und overall heat transfer coefficient $k \cdot A$ for different fin pitches during the on phase of one cycle with frosting (PLC-A).

3.3. Optimal Fin Pitch and Overall Efficiency

Figure 6 displays the $\overline{COP}_{\text{Cycle}}$ for all test points and the resulting Seasonal Coefficient of Performance ($SCOP$). The analysis shows that the optimal fin pitch is highly dependent on the operating conditions.

For the frosting test points (PLC-E, PLC-A, PLC-B), the optimal fin pitch increases as ambient temperature and humidity rise.

- PLC-E (Low Temperature): With low absolute humidity, the main challenge is heat transfer. Maximizing $k \cdot A$ is crucial, making a small fin pitch (2 mm) optimal.
- PLC-B (High Humidity): With high absolute humidity, frost growth makes airflow blockage the dominant penalty. A larger, more robust fin pitch (4 mm) is optimal as it maintains airflow for longer.
- The performance gap between the best and worst fin pitches widens with increased frosting, from less than 5 % at PLC-E to almost 10 % at PLC-B, confirming that frost amplifies the inherent loss mechanisms.

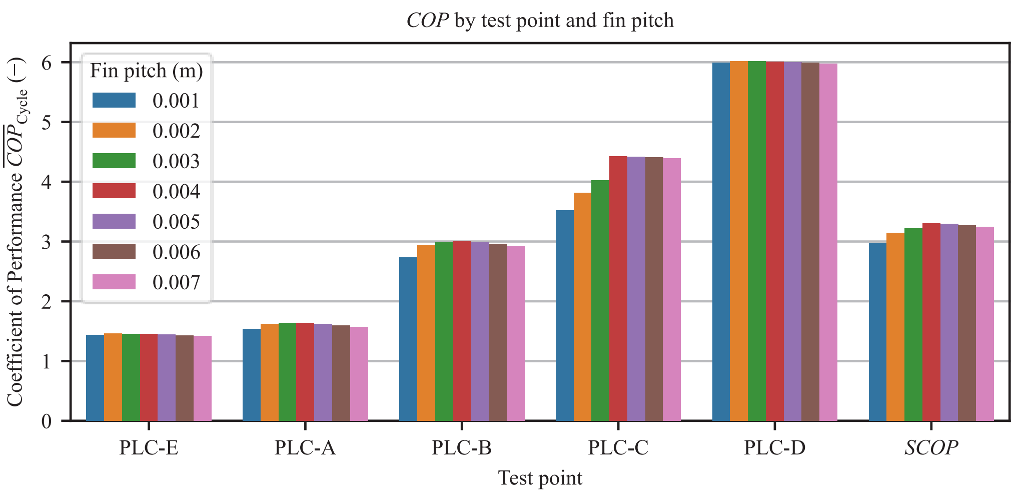

Figure 6. $\overline{COP}_{\text{Cycle}}$ for analyzed test points compared to $SCOP$. A fin pitch of 4 mm results in the highest $SCOP$.

At test point PLC-C, fin pitches from 1 to 3 mm experience frost growth and require defrosting. For pitches of 4 mm and larger, the higher fin temperature prevents sustained frost accumulation after an initial settling period, eliminating defrost cycles and yielding a higher $\overline{COP}_{\text{Cycle}}$. At the non-frosting point PLC-D, efficiency differences are smaller, and the optimum is a 2 mm pitch. Further analysis of the positive impact of condensation could be beneficial.

Considering the weighted importance of all operating conditions, particularly PLC-B and PLC-C, a fin pitch of 4 mm emerges as the best system-level compromise, resulting in the highest $SCOP$.

3.4. Impact of Placement Scenario (Humidity Variation)

Varying the relative humidity alters frost growth rates, which in turn affects the refrigerant cycle state and control decisions. For the primary frosting points (PLC-E, PLC-A, PLC-B), a 10 % decrease in relative humidity leads to less frost and higher values of $\overline{COP}_{\text{Cycle}}$, while a 10 % increase has the opposite effect. These $\overline{COP}_{\text{Cycle}}$ changes are relatively small, generally less than 2 %.

An exception occurs at PLC-C with a 3 mm fin pitch. A 10 % increase in relative humidity results in a $\overline{COP}_{\text{Cycle}}$ increase of over 10 %. Here, the control system manages to maintain a stable, non-growing frost layer for 15 hours, avoiding defrost initiation. This demonstrates that the control strategy has a major impact on performance and warrants further investigation. At the condensation-only point PLC-D, higher humidity leads to more latent heat transfer, slightly increasing the $\overline{COP}_{\text{Cycle}}$ by less than 1 %.

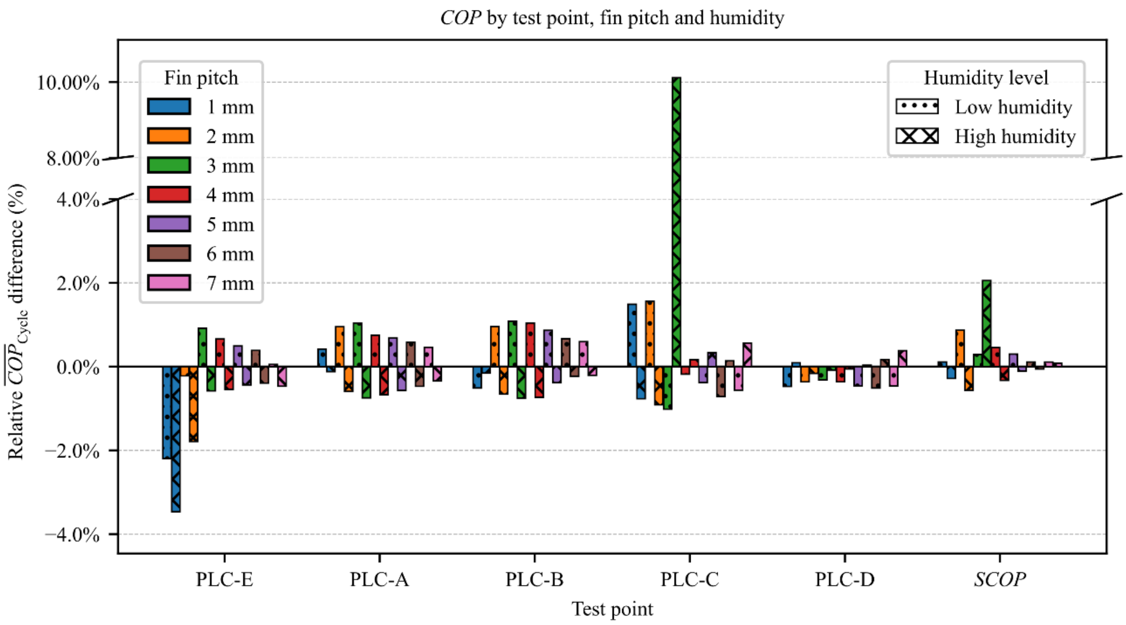

Figure 7. Comparison of $\overline{COP}_{\text{Cycle}}$ by test point and fin pitch with higher and lower relative humidity compared to test points in Table 4.

4. Discussion and Limitations

This study confirms that an integrated approach is essential, as the optimal fin pitch varies significantly with operating conditions. Achieving high efficiency requires optimizing for the most frequently occurring conditions, which the $SCOP$ metric helps to identify. Using a well-tuned controller that accounts for frost formation can further improve efficiency in real-world operation. The fan control strategy could be investigated further; for example, higher fan speeds might create denser frost and slow the rate of airflow decrease, though at the cost of increased noise. Future work could improve the design by finding a fundamental balance between the thermal and fluid-dynamic losses.

The conclusions are subject to the following limitations:

- **Idealized Models:** The simulation assumes uniform airflow and frost distribution. In reality, airflow is non-uniform (higher in the center, lower in the corners), which would cause non-uniform frost growth. This would likely create local areas where one loss mechanism strongly dominates.
- **Model Calibration:** The refrigerant cycle and frost models are fully physical models, thus, capturing the physical interactions of an integrated design procedure. However, the models were not

calibrated against experimental data of a dedicated heat pump test bench, yet. A physical test bench is needed to test different evaporator designs under various conditions to validate the quantitative accuracy of these simulation results.

5. Conclusion

This study confirms the fundamental design trade-off in evaporator fin pitch, where the ideal geometry is predetermined by the dominant loss mechanism. Smaller pitches (e.g., 2 mm) are optimal under non-frosting conditions by maximizing heat transfer surface area. However, as frosting becomes severe, the penalty from airflow blockage dominates, making a larger, frost-tolerant pitch (e.g., 4 mm) superior as it maintains airflow and delays defrost cycles.

By using the Seasonal Coefficient of Performance to integrate performance across a full range of operating point conditions, this work identifies a 4 mm fin pitch as the most robust compromise for maximizing year-round system efficiency. This result underscores the importance of employing seasonal metrics over single rated-point analyses to design systems that are efficient and resilient in real-world applications.

To build upon these simulation-based findings, our future work will proceed along parallel tracks of experimental validation and model development. We design and construct a dedicated evaporator test bench to provide data for model calibration under controlled dynamic conditions.

Concurrently, we develop more realistic models for the air-side pressure drop and the thermal insulation effect of the frost layer, moving beyond simplified modeling assumptions.

6. Nomenclature

Abbreviations

2MM	Two mass model
ASHP	Air source heat pump
BMWE	German Federal Ministry for Economic Affairs and Energy
BUH	backup heater
FMU	Functional mockup unit
HX	Heat exchanger
PLC	Test point

Formula symbols

d_{fin}	Fin pitch (m)
$k \cdot A$	Overall heat transfer coefficient (W/K)
$\overline{COP}_{\mathrm{Cycle}}$	Cycle averaged Coefficient of Performance (−)
h_{T_i}	Number of bin hours per year (−)
$\dot{m}_{\mathrm{water}}$	Mass flow rate of water (kg/s)
P_{BUH}	Electrical power consumption of backup heater (W)
P_{Comp}	Electrical power consumption of compressor (W)
P_{Fan}	Electrical power consumption of Fan (W)
P_{Pump}	Electrical power consumption of pump (W)
$\dot{Q}_{\mathrm{Cond}}$	Condenser heating power (W)
Q_{total,T_i}	Total delivered heat during a cycle (Wh)
$SCOP$	Seasonal Coefficient of Performance (−)
T_i	Temperature of test point (°C)
T_{ret}	Return temperature (°C)
T_{sup}	Supply temperature (°C)
$T_{\mathrm{sup,hp}}$	Supply temperature after heat pump (°C)
$T_{\mathrm{sup,set}}$	Set-Supply temperature (°C)
u_{EEV}	Opening of expansion valve (%)
$\dot{V}_{\mathrm{air}}$	Volume Flow Rate of air ($\mathrm{m^3/s}$)
W_{total,T_i}	Total work consumed during cycle (Wh)
ΔT_{SH}	Superheat (K)
φ	Relative Humidity (%)

Acknowledgments

The authors gratefully acknowledge the financial support by the German Federal Ministry for Economic Affairs and Energy (BMWE), promotional reference 03EN4113B.

Bibliography

[1] G. Uguen and S. Azau, 'European heat pump market report'. European Heat Pump Association, 2025. Accessed: Nov. 08, 2025. [Online]. Available: https://ehpa.org/news-and-resources/press-releases/heat-pump-sales-14-times-greater-in-lead-countries/

[2] L. Ma, Y. Sun, F. Wang, M. Wang, S. Zhang, and Z. Wang, 'Advancements in anti-frosting and defrosting techniques for air source heat pumps: A comprehensive review of recent progress', *Applied Energy*, vol. 377, p. 124538, 2025, doi: 10.1016/j.apenergy.2024.124358.

[3] C. Höges *et al.*, 'Low-GWP refrigerants in heat pumps: An experimental investigation of the influence of an internal heat exchanger', *Energy Conversion and Management: X*, vol. 24, p. 100704, Oct. 2024, doi: 10.1016/j.ecmx.2024.100704.

[4] F. Will, M. G. Ellinger, T. Klebig, C. Vering, and D. Müller, 'Experimental investigation of efficient and safe heat pump operation with model-based superheat control', *J. Phys.: Conf. Ser.*, vol. 3140, no. 2, p. 022012, Nov. 2025, doi: 10.1088/1742-6596/3140/2/022012.

[5] J. Klingebiel, M. Hassan, V. Venzik, C. Vering, and D. Müller, 'Efficiency comparison between defrosting methods: A laboratory study on reverse-cycle defrosting, electric heating defrosting, and warm brine defrosting', *Applied Thermal Engineering*, vol. 233, p. 121072, Oct. 2023, doi: 10.1016/j.applthermaleng.2023.121072.

[6] J. Klingebiel *et al.*, 'Optimal Defrost Initiation for Air-Source Heat Pumps: Evaluating the Improvement Potential of Common Defrosting Controllers', *Energy*, vol. 324, Jun. 2025, doi: 10.2139/ssrn.5123163.

[7] C. Fan *et al.*, 'Retarding frosting of an air source heat pump by using vapor-bypassed evaporation technique', *International Journal of Refrigeration*, vol. 127, pp. 69–77, Jul. 2021, doi: 10.1016/j.ijrefrig.2021.03.014.

[8] Optimized Thermal Systems, *CoilDesigner®*. (2016). Beltsville, MD. Accessed: Nov. 08, 2025. [Online]. Available: https://optimizedthermalsystems.com/coildesigner/

[9] P. Domanski and D. Yashar, *EVAP-COND, Version 4*. (Apr. 28, 2010). National Institute of Standards and Technology, Gaithersburg, MD. Accessed: Nov. 08, 2025. [Online]. Available: https://www.nist.gov/services-resources/software/evap-cond

[10] Corberán J. M. and J. N. González, *IMST-ART*. (2009). Universidad Politécnica de Valencia, Valencia.

[11] L. Hu, T. Xiong, Y. Yang, G. Liu, and G. Yan, 'Recent advances in refrigerant circuitry optimization of fin-and-tube heat exchangers for air source heat pump systems', *Energy*, vol. 333, p. 137443, Oct. 2025, doi: 10.1016/j.energy.2025.137443.

[12] W. Hou, H. Liu, J. E. Braun, and D. Ziviani, 'Machine learning-assisted multi-objective optimization for finned-tube heat exchangers in a reversible air-source heat pump with R454C', *Applied Thermal Engineering*, vol. 280, p. 128364, Dec. 2025, doi: 10.1016/j.applthermaleng.2025.128364.

[13] N. Jing, Y. Xia, Q. Ding, Y. Chen, Z. Wang, and X. Zhang, 'Simulation and Optimization Study on the Performance of Fin-and-Tube Heat Exchanger', *Sustainability*, vol. 15, no. 15, p. 11587, Jul. 2023, doi: 10.3390/su151511587.

[14] C. Vering, F. Wüllhorst, P. Mehrfeld, and D. Müller, 'Towards an integrated design of heat pump systems: Application of process intensification using two-stage optimization', *Energy Conversion and Management*, vol. 250, p. 114888, Dec. 2021, doi: 10.1016/j.enconman.2021.114888.

[15] R. S. Ribeiro, D. L. Da Silva, and C. J. L. Hermes, 'Optimal design of fan-supplied tube-fin evaporators subjected to frosting conditions aiming at minimum energy consumption', *J Braz. Soc. Mech. Sci. Eng.*, vol. 40, no. 10, p. 479, Oct. 2018, doi: 10.1007/s40430-018-1401-4.

[16] D.-K. Yang, K.-S. Lee, and S. Song, 'Fin spacing optimization of a fin-tube heat exchanger under frosting conditions', *International Journal of Heat and Mass Transfer*, vol. 49, no. 15–16, pp. 2619–2625, Jul. 2006, doi: 10.1016/j.ijheatmasstransfer.2006.01.016.

[17] TLK Thermo GmbH, *TIL Suite - Modellierung und Simulation*. Accessed: Nov. 08, 2025. [Online]. Available: https://www.tlk-thermo.com/de/software/til-suite

[18] M. Farzaneh, N. Zgheib, and S. A. Sherif, 'Numerical simulation of frost formation and heat transfer on fin-and-tube heat exchangers in turbulent cross-flow', *Phil. Trans. R. Soc. A.*, vol. 383, p. 23, Jul. 2025, doi: https://doi.org/10.1098/rsta.2024.0366.

[19] J. K. Jensen, S. O. K. Hansen, and W. B. Markussen, 'Simulating an evaporator field for large-scale air-source heat pumps subjected to frosting and defrosting.', in *Refrigeration Science and Technology Proceedings*, Paris France: International Institute of Refrigeration (IIR), 25.08 2025, pp. 950–961. doi: 10.18462/IIR.ICR.2023.0363.

[20] D. Seker, H. Karatas, and N. Egrican, 'Frost formation on fin-and-tube heat exchangers. Part I—Modeling of frost formation on fin-and-tube heat exchangers', *International Journal of Refrigeration*, vol. 27, no. 4, pp. 367–374, Jun. 2004, doi: 10.1016/j.ijrefrig.2003.12.003.

[21] S. Göbel *et al.*, 'From Refrigerant Cycle to Product Testing: Fostering Innovation in Heat Pump Controllers through Real-Life Testing', in *Proceedings of the 15th IEA Heat Pump Conference*, Wien, Jun. 2026.

[22] 'EN 14511:2018, Air conditioners, liquid chilling packages and heat pumps for space heating and cooling and process chillers, with electrically driven compressors: Terms and definitions', CEN/TC 113, Bruxelles, Belgium, Mar. 2018.

[23] S. Haaf, 'Wärmeübertragung in Luftkühlern', in *Wärmeaustauscher*, F. Steimle, K. Stephan, S. Haaf, H. G. Hirschberg, E. Hofmann, H. Lotz, H. Nawothnig, P. Paikert, B. Slipčević, H. Schnell, A. Schuster, and A. Schütz, Eds., Berlin, Heidelberg: Springer Berlin Heidelberg, 1988, pp. 435–491. doi: 10.1007/978-3-642-82522-4_13.

[24] R. O'Hegarty, O. Kinnane, D. Lennon, and S. Colclough, 'Air-to-water heat pumps: Review and analysis of the performance gap between in-use and product rated performance', *Renewable and Sustainable Energy Reviews*, vol. 155, p. 111887, Mar. 2022, doi: 10.1016/j.rser.2021.111887.